DOI: 10.1002/chem.200903380

Synthesis of Hierarchical Macro-/Mesoporous Solid-Solution Photocatalysts by a Polymerization–Carbonization–Oxidation Route: The Case of $Ce_{0.49}Zr_{0.37}Bi_{0.14}O_{1.93}$

Guangcheng Xi and Jinhua Ye*[a]

Abstract: A hierarchical macro-/mesoporous $Ce_{0.49}Zr_{0.37}Bi_{0.14}O_{1.93}$ solid-solution network has been synthesized on a large scale by means of a simple and general polymerization–carbonization–oxidation synthetic route. The as-prepared product has been characterized by SEM, XRD, TEM, BET surface area measurement, UV/Vis diffuse-reflectance spectroscopy, energy-dispersive X-ray spectroscopy (EDS), and photoelectrochemistry measurements. The photocatalytic activity of the product has been demonstrated through the photocatalytic degradation of methyl orange. Structural characterization has indicated that the hierarchical macro-/mesoporous solid-solution network not only contains numerous macropores, but also possesses an interior mesoporous structure. The mesopore size and BET surface area of the network have been measured as 2–25 nm and 140.5 m^2g^{-1}, respectively. The hierarchical macro-/mesoporous solid-solution network with open and accessible pores was found to be well-preserved after calcination at 800 °C, indicating especially high thermal stability. Due to its high specific surface area, the synergistic effect of the coupling of macropores and mesopores, and its high crystallinity, the $Ce_{0.49}Zr_{0.37}Bi_{0.14}O_{1.93}$ solid-solution material shows a strong structure-induced enhancement of visible-light harvest and exhibits significantly improved visible-light photocatalytic activity in the photodegradation of methyl orange compared with those of its other forms, such as mesoporous hollow spheres and bulk particles.

Keywords: crystal growth · macropores · mesoporous materials · nanostructures · photocatalysis

Introduction

Semiconductor photocatalysts have attracted much research attention owing to their applications in tackling current environmental and energy issues, especially for the splitting of water to supply clean hydrogen energy and in water remediation by the removal of harmful organic pollutants.[1–5] To date, TiO_2 has been the best and the most widely used photocatalyst because of its excellent quantum efficiency, high chemical stability, and low toxicity.[6] However, its relatively wide band gap of 3.2 eV requires UV light for effective photocatalysis, thus severely limiting its practical utility.[7] Although anion- and cation-doped TiO_2 with visible-light activity have been prepared, their photocatalytic activities under visible-light irradiation are comparatively low.[8] Recently, increasing attention has been paid to the development of new visible-light-active photocatalysts.[9–15] Among these, solid-solution semiconductors with tunable electronic structures are of particular interest because of their unique properties that are unattainable from the individual constituent materials. Recently, Zou et al. synthesized $In_{0.9}Ni_{0.1}TaO_4$ solid-solution photocatalysts, which served to split pure water into H_2 and O_2 under visible-light irradiation.[16] Domen and co-workers successfully prepared $(Ga_{1-x}Zn_x)$-$(N_{1-x}O_x)$ solid solution with high visible-light photocatalytic activity.[17] More recently, our group synthesized visible-light-active $(Ag_{0.75}Sr_{0.25})(Nb_{0.75}Ti_{0.25})O_3$ solid solution, which was effective in the photocatalytic decomposition of CH_3CHO into CO_2 and H_2O.[18] However, the above-mentioned solid-solution photocatalysts have generally been prepared by traditional solid-state reaction methods, leading to

[a] Dr. G. Xi, Prof. J. Ye
International Center for Materials Nanoarchitectonics
and Photocatalytic Materials Center
National Institute for Materials Science
1-2-1 Sengen, Tsukuba, Ibaraki 305-0047 (Japan)
Fax: (+81) 29-859-2601
E-mail: Jinhua.Ye@nims.go.jp

Supporting information for this article is available on the WWW under http://dx.doi.org/10.1002/chem.200903380: XRD pattern of the as-synthesized crosslinked Ce-Zr-Bi-GCP composite network; SEM image, nitrogen adsorption–desorption isotherm plot, and UV/Vis spectrum of nonporous $Ce_{0.49}Zr_{0.37}Bi_{0.14}O_{1.93}$ solid solution.

the formation of photocatalysts with low specific surface areas, which severely limit their photocatalytic efficiencies.

Since photocatalytic reactions occur at the surfaces of catalysts, a nanosized photocatalyst will greatly increase the reaction rate due to the increased surface area.[19] Unfortunately, nanocrystals of very small size generally tend to aggregate during aging, resulting in a reduction of the active surface area.[20] Furthermore, the separation of these nanocrystals from treated water is very difficult and energy-consuming, so that their usefulness is limited in practical applications. Therefore, the development of an effective synthesis of a visible-light-sensitive photocatalyst that is stable with respect to aggregation, easily separated, and that has a large surface exposure area is still one of the most important tasks for practical applications.

Hierarchical macro-/mesoporous (HMM) structural materials are able to efficiently absorb guest species and transport them to framework binding sites by virtue of their textural mesopores, intrinsic interconnected pore systems, and high specific surface areas.[21–24] Furthermore, the hierarchical porous structure can more effectively absorb visible-light energy through multiple reflections of visible light within its interior cavities.[25,26] Several research groups have reported the preparation of inorganic macro-/mesoporous materials by using various template-based methods, employing, for example, surfactants, emulsion droplets, and colloidal crystals.[27–29] However, multicomponent solid-solution oxides with HMM structure have seldom been reported.

HMM solid-solution photocatalysts that combine the advantages of porous structural control with a tunable electronic structure can be envisaged as being more promising for visible-light-driven photocatalysis. Herein, we report the synthesis of an effective visible-light-active photocatalyst, HMM $Ce_{0.49}Zr_{0.37}Bi_{0.14}O_{1.93}$ solid-solution network, by a facile and low-cost polymerization–carbonization–oxidation route. The obtained material combines high specific surface area, HMM structure, and high crystallinity, as a result of which it shows a strong structure-induced enhancement of visible-light harvest and exhibits a significantly improved visible-light photocatalytic activity in the photodegradation of methyl orange (MO) compared with its other material forms, such as mesoporous hollow spheres and bulk particles. In addition, the micrometer-scale outline of this photocatalyst allows its easy separation and recovery. Therefore, the resulting HMM $Ce_{0.49}Zr_{0.37}Bi_{0.14}O_{1.93}$ solid solution may be an attractive new photocatalyst for environmental remediation.

Results and Discussion

Scheme 1 illustrates the formation process of the HMM $Ce_{0.49}Zr_{0.37}Bi_{0.14}O_{1.93}$ solid-solution network. In the first step, glucose, cetyltrimethylammonium bromide (CTAB), $Ce(SO_4)_2$, $Bi(NO_3)_3$, and $ZrO(NO_3)_2$ were added to distilled water (100 mL). To avoid hydrolysis of the transition-metal ions in the solution, citric acid (CA) was selected as the chelating agent and acid because of its high cooperativity with metal ions and appropriate acidity. After stirring for 20 min, a transparent yellowish-green solution was formed. In the second step, glucose monomer was gradually transformed into a crosslinked glucose-derived carbon-rich polysaccharide (GCP) network through polymerization and carbonization reactions of glucose molecules under hydrothermal conditions.[30] It is well known that such GCP contains abundant hydroxyl (OH) and carbonyl (C=O) functional groups and mesopores in the carbonaceous branches.[31] Therefore, metal cations (Zr^{4+}, Ce^{4+}, and Bi^{3+}) would diffuse into the carbonaceous branches through capillary action and become coordinated by the OH and C=O groups, forming a crosslinked Ce-Zr-Bi-GCP composite network. The crosslinked Ce-Zr-Bi-GCP composite network serves as a precursor and template for the formation of the HMM solid solution. In the third step, the as-synthesized crosslinked Ce-Zr-Bi-GCP composite network is oxidized in air at 800 °C for 1 h. In the oxidation process, the carbon components contained in the crosslinked Ce-Zr-Bi-GCP composite are removed and the remaining structure containing the metal cations is compacted, densified, and crosslinked to form mesoporous solid-solution nanocrystals. This process is similar to the formation of mesoporous metal oxide hollow spheres reported by Li et al.[30c] After the oxidation process, the solid-solution product obtained partly retains the network-like morphology of the precursor, but with reduced size.

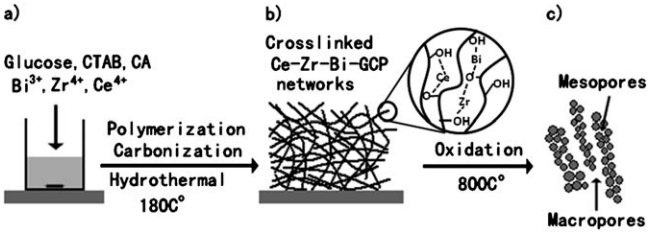

Scheme 1. Schematic representation of the procedure for obtaining the hierarchical macro-/mesoporous $Ce_{0.49}Zr_{0.37}Bi_{0.14}O_{1.93}$ solid solution.

A general overview SEM image in Figure 1a shows that the as-synthesized Ce-Zr-Bi-GCP network precursor was composed of flexible nanowires of diameter 150–200 nm and lengths of up to 100 μm. A high-magnification SEM image (Figure 1b) shows that the nanowires became linked and entangled with each other, forming a network structure. The XRD pattern showed the crosslinked network to be amorphous (Figure S1 in the Supporting Information). A clear broad peak at 10–40°, corresponding to amorphous carbon structures, was observed.[23] Figure 1c shows a low-magnification SEM image of a $Ce_{0.49}Zr_{0.37}Bi_{0.14}O_{1.93}$ solid solution obtained by oxidizing the pre-synthesized crosslinked Ce-Zr-Bi-GCP network precursor. It can be seen that the as-synthesized solid-solution particles have a micrometer-scale outline, suggesting that they should be easily recoverable from treated water. Figure 1d shows a magnified SEM image of a solid-solution particle, which clearly displays the porous structure of the as-synthesized solid-solution sample.

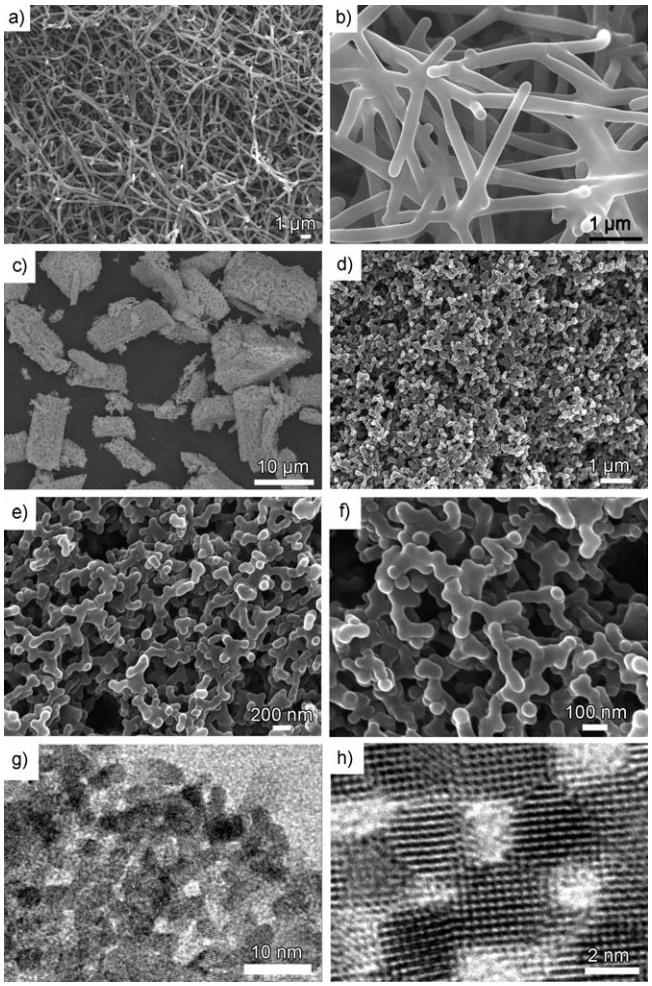

Figure 1. a) Low- and b) high-magnification SEM images of the crosslinked Ce-Zr-Bi-GCP network; c) low- and d)–f) high-magnification SEM images of the HMM $Ce_{0.49}Zr_{0.37}Bi_{0.14}O_{1.93}$ solid-solution network; g) TEM and h) HRTEM images of the HMM $Ce_{0.49}Zr_{0.37}Bi_{0.14}O_{1.93}$ solid-solution network.

Figure 1e and f show further high-magnification SEM images of the solid-solution sample. The surface of the particles is very rough and composed of numerous self-supported macropores with pore diameters of 50–400 nm. Furthermore, from the two high-magnification SEM images, we can see that the as-synthesized solid-solution sample partly retained the morphology of the crosslinked Ce-Zr-Bi-GCP precursor, maintaining a complicated network structure. A TEM image (Figure 1g) indicates that the branches of the network are composed of mesoporous structures formed by the random attachment of nanoparticles with sizes in the range 3–7 nm. Figure 1h displays an HRTEM image taken on the edge of a branch of the network, which clearly demonstrates that the nanoparticles were highly crystalline and that numerous mesopores were present.

To investigate the phase purity of the as-synthesized HMM solid solution, a sample was subjected to XRD analysis, and the results are shown in Figure 2. All of the diffraction peaks match well those of the corresponding CeO_2-

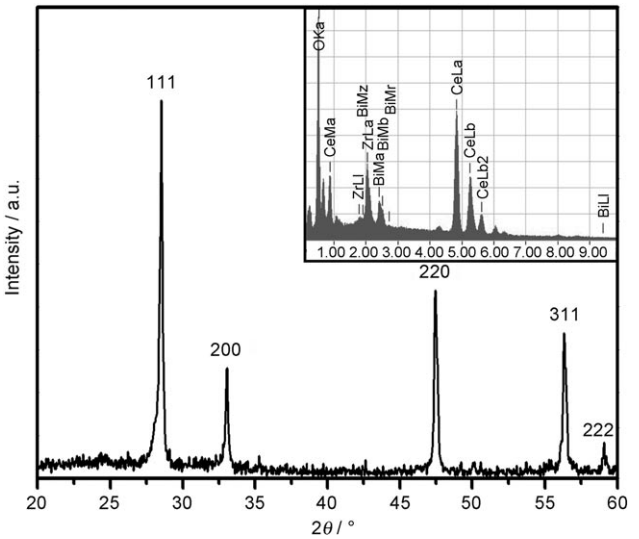

Figure 2. The XRD pattern of the as-synthesized HMM $Ce_{0.49}Zr_{0.37}Bi_{0.14}O_{1.93}$ solid solution (JPCDS no.: 38-1439). Inset: EDS spectrum of the HMM $Ce_{0.49}Zr_{0.37}Bi_{0.14}O_{1.93}$ solid solution.

ZrO_2 solid solution of fluorite-type structure (JPCDS no. 38-1439), and no Bi_2O_3 diffraction peaks are detected, which suggests that Bi^{3+} ions completely dissolved in the CeO_2-ZrO_2 lattice to form a pure solid solution of fluorite-type structure. Energy-dispersive X-ray spectroscopy (EDS) indicated that the porous sample was composed of Ce, Zr, Bi, and O (inset in Figure 2). Based on the calculated peak areas, the atomic ratio of Ce/Zr/Bi/O was about 0.49:0.37:0.14:1.93. It should be noted that Bi could not be dissolved in the solid solution in indefinite amounts, but that the proportion of the Bi component could not exceed 0.19 in the body of the solid solution. If the proportion of the Bi component were higher than 0.19, the final product would be contaminated with Bi_2O_3.

The specific surface area of the as-synthesized HMM $Ce_{0.49}Zr_{0.37}Bi_{0.14}O_{1.93}$ solid-solution network was investigated by obtaining nitrogen adsorption and desorption isotherms (Figure 3). The specific surface area of the sample was thereby estimated as 140.5 $m^2 g^{-1}$. The pore-size distribution (inset in Figure 3) was determined from the desorption branch of the isotherm using the Barrett–Joyner–Halenda (BJH) method. The average pore diameter of the sample was 2–25 nm (mesopores and macropores), which may be attributed to the mesoporous branches and some macropores with small diameters. The larger macropores (shown in Figure 1d–f) could not be seen because the diameter of these pores was beyond the measurement range. In comparison, the specific surface area of a nonporous $Ce_{0.49}Zr_{0.37}Bi_{0.14}O_{1.93}$ solid solution prepared by a traditional solid-state reaction was only 6.5 $m^2 g^{-1}$ (Figures S2–S4 in the Supporting Information).

The photophysical properties of the HMM $Ce_{0.49}Zr_{0.37}Bi_{0.14}O_{1.93}$ network were investigated by UV/Vis diffuse-reflectance spectroscopy (Figure 4). The spectra of

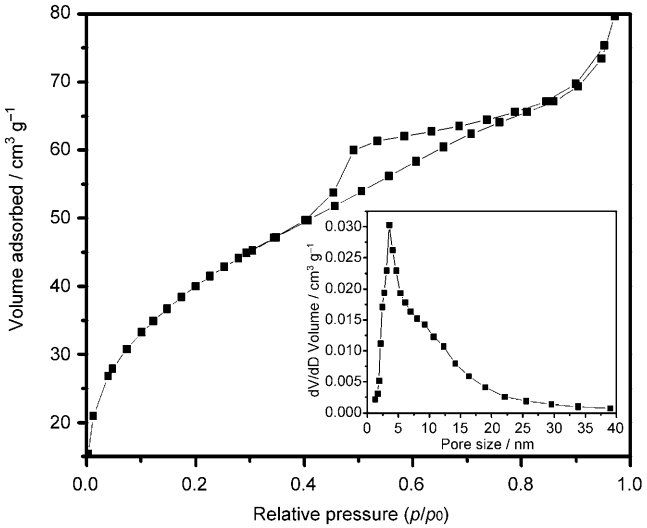

Figure 3. Nitrogen adsorption–desorption isotherm plot for the HMM $Ce_{0.49}Zr_{0.37}Bi_{0.14}O_{1.93}$ solid solution. Inset: Barrett–Joyner–Halenda (BJH) pore-size distribution plot of the HMM $Ce_{0.49}Zr_{0.37}Bi_{0.14}O_{1.93}$ solid-solution sample.

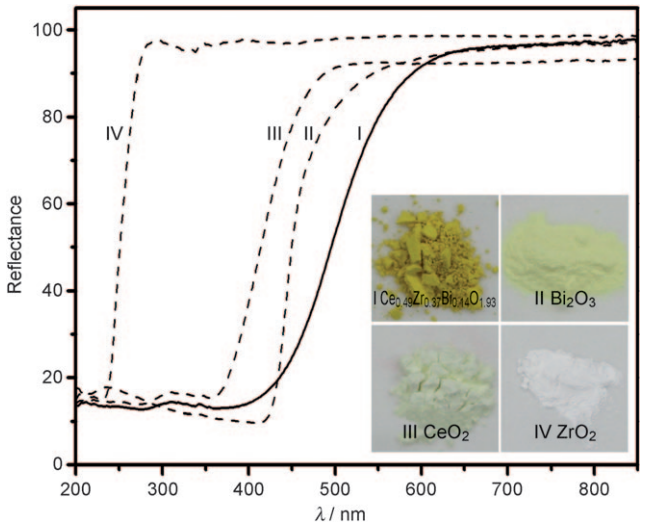

Figure 4. UV/Vis diffuse-reflectance spectra of HMM $Ce_{0.49}Zr_{0.37}Bi_{0.14}O_{1.93}$, as well as of CeO_2, ZrO_2, and Bi_2O_3 samples. The insets show pictures of the samples.

commercial CeO_2, ZrO_2, and Bi_2O_3 powders are also shown for comparison. The absorption edges of the HMM $Ce_{0.49}Zr_{0.37}Bi_{0.14}O_{1.93}$ are seen to shift remarkably to longer wavelengths compared with those of the monocomponent oxides, and as a result the HMM $Ce_{0.49}Zr_{0.37}Bi_{0.14}O_{1.93}$ shows clear light absorption in the visible region. The band gap of the HMM $Ce_{0.49}Zr_{0.37}Bi_{0.14}O_{1.93}$ solid solution is 2.5 eV. From the insets in Figure 4, one can see that the HMM $Ce_{0.49}Zr_{0.37}Bi_{0.14}O_{1.93}$ solid-solution network is vivid yellow, whereas the commercial CeO_2, ZrO_2, and Bi_2O_3 powders are ivory yellow, white, and pale yellow, respectively. From the UV/Vis spectra and the color changes of the samples, it is clear that the as-synthesized HMM sample was a uniform solid solution rather than a mixture of CeO_2, ZrO_2, and Bi_2O_3.

CTAB has been identified as playing an important role in the present synthesis of the crosslinked Ce-Zr-Bi-GCP composite network precursor. In a parallel experiment, in which CTAB was omitted from the reaction mixture, numerous Ce-Zr-Bi-GCP microspheres were obtained and no crosslinked Ce-Zr-Bi-GCP composite network was detected (Figure 5a). As an anionic surfactant, CTAB has been demonstrated to be an excellent soft template for the synthesis of Ag and Au nanorods and nanowires.[32,33] On the basis of previous work and our own experimental observations, one possible function of CTAB in the present synthetic method might be to generate large numbers of rod-like micelles in aqueous solution, which may act as soft templates for the formation of crosslinked GCP networks while also stabilizing the crosslinked branches. Interestingly, when the Ce-Zr-Bi-GCP microspheres were calcined and oxidized in air at 800 °C for 1 h, closed and porous $Ce_{0.49}Zr_{0.37}Bi_{0.14}O_{1.93}$ solid-solution hollow spheres were synthesized, which were similar to the metal oxide hollow spheres reported previously.[34] Figure 5b and c show SEM images of the porous $Ce_{0.49}Zr_{0.37}Bi_{0.14}O_{1.93}$ hollow spheres at different magnifications. Figure 5b shows a low-magnification SEM image of the sample, which indicates that the product was composed of a large quantity of hollow spheres. The diameters of these hollow spheres were in the range 400–600 nm and the thickness of the shells was about 30–50 nm. The porous structure of the hollow spheres can be easily seen in FESEM images recorded at a higher magnification (Figure 5c). As shown in Figure 5c, the sample exhibited a unique porous surface. BET measurements revealed the specific surface area and

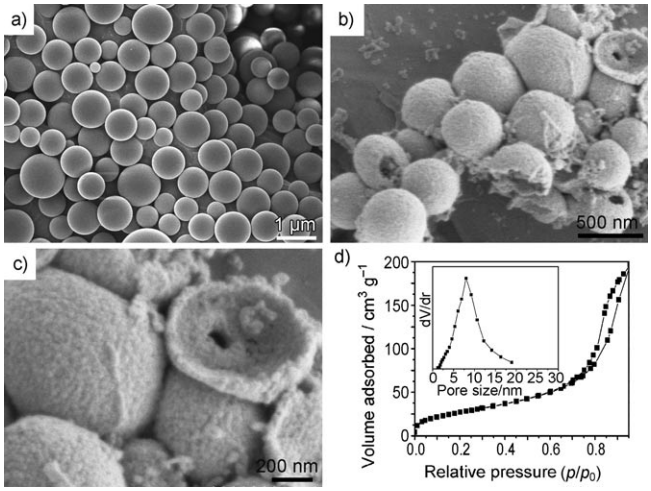

Figure 5. a) SEM image of the as-synthesized Ce-Zr-Bi-GCP microspheres; b), c) mesoporous $Ce_{0.49}Zr_{0.37}Bi_{0.14}O_{1.93}$ solid-solution hollow spheres obtained by calcining the Ce-Zr-Bi-GCP microspheres in air at 800 °C for 1 h; d) nitrogen adsorption–desorption isotherm plot for the mesoporous $Ce_{0.49}Zr_{0.37}Bi_{0.14}O_{1.93}$ hollow spheres. Inset: Barrett–Joyner–Halenda (BJH) pore-size distribution plot for the mesoporous $Ce_{0.49}Zr_{0.37}Bi_{0.14}O_{1.93}$ hollow spheres.

the average pore diameter of the hollow spheres to be 162.7 $m^2 g^{-1}$ and 8 nm, respectively (Figure 5d).

The photoelectrochemical properties of the HMM $Ce_{0.49}Zr_{0.37}Bi_{0.14}O_{1.93}$ solid-solution network were also investigated. Figure 6 shows potentiodynamic scans (10 $mV s^{-1}$) obtained under chopped illumination for the HMM network, mesoporous hollow spheres, and a nonporous solid-solution sample. The electrolyte was 0.1 M Na_2SO_4 without any additive. It is clear that an enhanced photocurrent was obtained over the entire potential range for the HMM $Ce_{0.49}Zr_{0.37}Bi_{0.14}O_{1.9}$ network. At 1.0 V, the photocurrent density of the HMM $Ce_{0.49}Zr_{0.37}Bi_{0.14}O_{1.93}$ network sample was more than four times the value for the nonporous sample. Furthermore, it can be seen that the photocurrent density of the HMM network sample was more than 1.5 times the value for the mesoporous hollow-sphere sample at 1.0 V. This is an interesting experimental observation, since the specific surface area of the HMM network was smaller than that of the mesoporous hollow spheres. Generally, a higher photocurrent density can be expected when the surface area of a material is increased. In the present case, the HMM network architecture results in a large effective surface area in close proximity to the electrolyte, thus enabling diffusive transport of photogenerated holes to oxidizable species in the electrolyte and improving the separation of photogenerated charges. Conversely, for the mesoporous hollow-sphere sample, the effective surface area in contact with the electrolyte is reduced because of the close-packed structure of the spherical shells, which may result in a reduced photocurrent density.

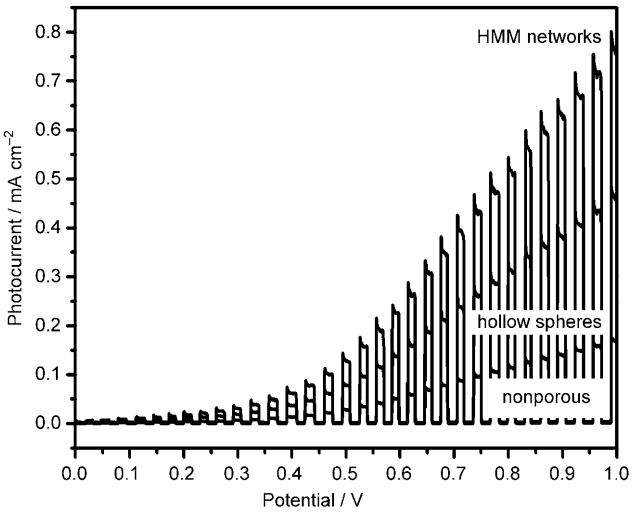

Figure 6. Potentiodynamic scans obtained under chopped illumination for the HMM network, mesoporous hollow spheres, and a nonporous solid-solution sample.

To demonstrate the potential application of the as-synthesized HMM $Ce_{0.49}Zr_{0.37}Bi_{0.14}O_{1.93}$ solid solution, its photocatalytic activity in the degradation of MO was investigated. The progress of the photodegradation with irradiation time was monitored by analyzing the UV/Vis spectra of aliquots of the reaction solution withdrawn at different time intervals. Figure 7 shows the optical absorption spectra of an aqueous solution of MO (initial concentration 8 $mg L^{-1}$; 100 mL) with 50 mg of the as-prepared HMM $Ce_{0.49}Zr_{0.37}Bi_{0.14}O_{1.93}$ solid solution measured after exposure to visible light ($\lambda > 420$ nm) for different durations. As is evident from Figure 7, the intensity of the characteristic absorption peak of MO gradually decreased with increasing exposure time, indicating photocatalytic degradation of the dye in the presence of HMM $Ce_{0.49}Zr_{0.37}Bi_{0.14}O_{1.93}$ solid solution. The characteristic absorption peak of MO had almost completely disappeared after about 1 h, which suggests that the as-synthesized HMM $Ce_{0.49}Zr_{0.37}Bi_{0.14}O_{1.93}$ solid solution served as a high-performance visible-light-activated photocatalyst. To evaluate the potential advantage of the HMM $Ce_{0.49}Zr_{0.37}Bi_{0.14}O_{1.93}$ solid-solution photocatalyst, further experiments were performed under the same conditions aimed at comparing the photocatalytic activities of the HMM sample and a nonporous $Ce_{0.49}Zr_{0.37}Bi_{0.14}O_{1.93}$ solid solution prepared by the traditional solid-state reaction route, respectively (Figure 8). It was observed that the photolysis of MO under visible-light irradiation was very slow in the absence of a photocatalyst. When using the nonporous $Ce_{0.49}Zr_{0.37}Bi_{0.14}O_{1.93}$ solid solution as the photocatalyst, the time required for complete photodegradation of the MO was more than 5 h. Furthermore, to evidence the synergistic effect of the coupling of macropores and mesopores contained in the HMM solid-solution network, the rate of photodegradation of MO observed in the presence of the HMM solid-solution network was compared with that observed in the presence of mesoporous $Ce_{0.49}Zr_{0.37}Bi_{0.14}O_{1.93}$ hollow

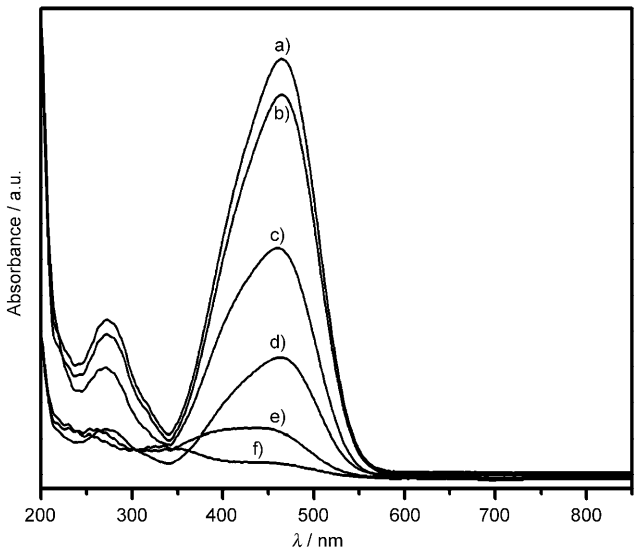

Figure 7. UV/Vis spectroscopic changes of an aqueous solution of MO upon irradiation in the presence of the HMM $Ce_{0.49}Zr_{0.37}Bi_{0.14}O_{1.93}$ solid-solution sample; a) original, b) dark for 30 min; light on for c) 15 min, d) 30 min, e) 45 min, and f) 60 min.

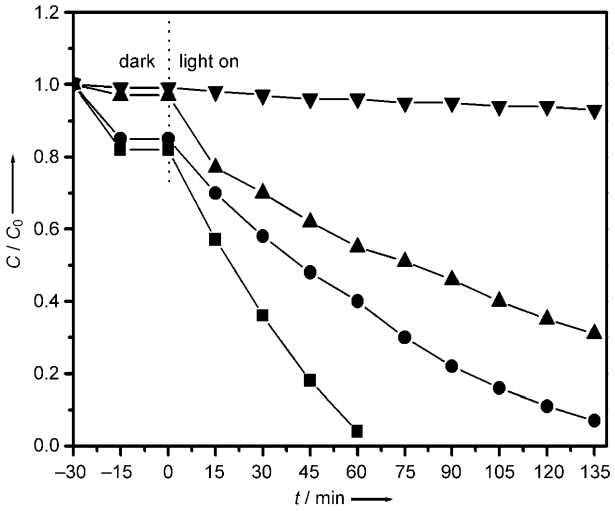

Figure 8. The photocatalytic degradation of MO in the presence of the HMM network (■), mesoporous hollow spheres (●), and a nonporous solid-solution sample (▲); ▼ = without photocatalyst.

spheres that contained only mesoporous structures. Interestingly, although the mesoporous $Ce_{0.49}Zr_{0.37}Bi_{0.14}O_{1.93}$ hollow spheres had a specific surface area ($162.7\ m^2g^{-1}$) greater than that of the HMM $Ce_{0.49}Zr_{0.37}Bi_{0.14}O_{1.93}$ ($140.5\ m^2g^{-1}$), their overall activity in MO photodegradation was lower than that of the latter, which suggests that the overall photocatalytic activity of the HMM $Ce_{0.49}Zr_{0.37}Bi_{0.14}O_{1.93}$ network is more directly related to its interior structure than its specific surface area. In other words, the synergistic effect of the coupling of macropores and mesopores plays an important role in the improvement of the photocatalytic performance of the solid-solution sample.

The higher photocatalytic activity of the HMM $Ce_{0.49}Zr_{0.37}Bi_{0.14}O_{1.93}$ solid-solution network can be explained by considering several factors. Firstly, the larger specific surface area: the specific area of the HMM $Ce_{0.49}Zr_{0.37}Bi_{0.14}O_{1.93}$ solid-solution network is $140.5\ m^2g^{-1}$, whereas that of the nonporous $Ce_{0.49}Zr_{0.37}Bi_{0.14}O_{1.93}$ solid solution is only $6.5\ m^2g^{-1}$. Clearly, more reactant adsorption/desorption sites are available in the HMM sample for catalytic reaction. Secondly, the superior structural characteristics, that is, the HMM structure, which serve to enhance the rapid diffusion of various reactants during the reaction. For photocatalysts with a large surface area and a HMM structure, rapid surface e^-/h^+ separation and rapid interfacial charge-carrier transfer are achieved, which decrease the bulk e^-/h^+ recombination.[25] In addition, the structure prevents the unwanted aggregation of nanoparticle clusters, which is also helpful in maintaining the high active surface area.

Conclusion

In summary, a polymerization–carbonization–oxidation method for the fabrication of HMM networks composed of $Ce_{0.49}Zr_{0.37}Bi_{0.14}O_{1.93}$ solid-solution nanocrystals has been demonstrated. A photocatalytic degradation study of MO revealed that the HMM $Ce_{0.49}Zr_{0.37}Bi_{0.14}O_{1.93}$ solid-solution network functions as a more efficient visible-light-activated photocatalyst than mesoporous hollow spheres or nonporous particles. The present approach to the fabrication of solid solutions of HMM structure is fast and facile. Furthermore, extension of this synthetic strategy to a general strategy for obtaining other solid solutions of HMM structure shows great promise. The present study has proved that designing solid solutions of HMM structure with high specific area and high crystallinity is a feasible approach for the development of highly efficient visible-light-activated semiconductor photocatalysts.

Experimental Section

Chemicals: Glucose ($C_6H_{12}O_6$), citric acid (CA), cerium sulfate ($Ce(SO_4)_2$), bismuth nitrate ($Bi(NO_3)_3$), zirconyl nitrate ($ZrONO_3$), cetyltrimethylammonium bromide (CTAB), ceria (CeO_2), bismuth oxide (Bi_2O_3), zirconia (ZrO_2), distilled water, and absolute ethanol. All reagents used were analytically pure, as purchased from Wako Chemical Reagent Company, and were used without further purification.

Preparation of crosslinked Ce-Zr-Bi-GCP composite nanowires: $Ce(SO_4)_2$ (0.49 mmol), $ZrONO_3$ (0.37 mmol), $BiNO_3$ (0.14 mmol), glucose (4 g), CTAB (0.5 g), and citric acid (3 g) were added to distilled water (100 mL) under mild stirring, whereupon a yellowish-green solution was formed. The solution was loaded into a Teflon-lined autoclave, which was then sealed, maintained at 180 °C for 24 h, and then allowed to cool to room temperature. The obtained black woolly mass was collected and rinsed once with absolute ethanol. It was then dried at 70 °C for 4 h.

Preparation of HMM $Ce_{0.49}Zr_{0.37}Bi_{0.14}O_{1.93}$ solid solution: The as-synthesized crosslinked Ce-Zr-Bi-GCP composite nanowires were heated from room temperature to 800 °C over a period of 8 h and annealed at 800 °C for a further 1 h to obtain the final yellow product.

Photocatalytic degradation of MO: The photocatalytic activity of the HMM $Ce_{0.49}Zr_{0.37}Bi_{0.14}O_{1.93}$ solid solution was evaluated by degradation of MO in aqueous solution under visible light from a 300 W Xe lamp (CERMAX LX-300; ILC Technology) equipped with an L42 cut-off filter (Hoya Optics) and a water filter. The photocatalyst (50 mg) was added to RhB aqueous solution (100 mL; $4\ mg\,L^{-1}$) in a Pyrex reactor at room temperature under air. Before the light was turned on, the solution was continuously stirred for 30 min in the dark to ensure the establishment of an adsorption–desorption equilibrium. The concentration of MO during the degradation was monitored colorimetrically using a UV/Vis spectrophotometer.

Photoelectrochemical measurements were carried out using a conventional three-electrode, single-compartment glass cell fitted with a synthesized quartz window in conjunction with a potentiostat. The quartz electrolytic cell was filled with 0.1 M Na_2SO_4. A solid-solution electrode served as the working electrode. The potential was swept linearly at a scan rate of $10\ mV\,s^{-1}$. The illuminated area of the working electrode was $1\ cm^2$. The aforementioned 300 W Xe lamp was used as the visible-light source. The counter and reference electrodes were a platinum-black wire and a saturated calomel electrode (SCE), respectively. Photoelectrochemical experiments were performed using a CHI-660B electrochemical system.

Characterization: XRD patterns of the products were recorded on a Rigaku (Japan) D/max-γA X-ray diffractometer employing graphite-monochromated $Cu_{K\alpha}$ radiation ($\lambda = 1.54178$ Å). SEM images and EDS data were recorded with a field-emission scanning electron microscope (JEOL-6700F). Samples for transmission electron microscopy (TEM) analysis were prepared by drying a drop of nanocrystal dispersion in absolute ethanol on an amorphous carbon-coated copper grid. High-resolu-

tion TEM (HRTEM) characterization, revealing particle sizes and shapes, was performed with a JEOL 2010 microscope operated at 200 kV. UV/Vis absorption spectra were recorded on a Shimadzu UV-2500 spectrophotometer. BET measurements were carried out on a Shimadzu Micromeritics apparatus.

Acknowledgements

This work was supported in part by the World Premier International Research Center Initiative (WPI Initiative) on Materials Nanoarchitectonics, the MEXT, and the Strategic International Cooperative Program, Science and Technology Agency, Japan.

[1] A. Fujishima, K. Honda, *Nature* **1972**, *238*, 37.
[2] B. O'Regan, M. Gratzel, *Nature* **1991**, *353*, 737.
[3] M. R. Hoffmann, S. T. Martin, W. Choi, D. W. Bahnemann, *Chem. Rev.* **1995**, *95*, 69.
[4] F. E. Osterloh, *Chem. Mater.* **2008**, *20*, 35.
[5] A. Kudo, Y. Miseki, *Chem. Soc. Rev.* **2009**, *38*, 253.
[6] G. K. Mor, H. E. Prakasam, O. K. Varghese, K. Shankar, C. A. Grimes, *Nano Lett.* **2007**, *7*, 2356.
[7] W. K. Ho, J. C. Yu, S. C. Lee, *Chem. Commun.* **2006**, 1115.
[8] a) R. Asahi, T. Morikawa, T. Ohwaki, K. Aoki, Y. Taga, *Science* **2001**, *293*, 269; b) U. M. Shahed, A. Mofareh, B. William, *Science* **2002**, *297*, 2243; c) S. Sakthivel, H. Kisch, *Angew. Chem.* **2003**, *115*, 5057; *Angew. Chem. Int. Ed.* **2003**, *42*, 4908.
[9] F. Gao, X. Y. Chen, K. B. Yin, S. Dong, Z. F. Ren, F. Yuan, T. Yu, Z. G. Zou, J. M. Liu, *Adv. Mater.* **2007**, *19*, 2889.
[10] C. Zhang, Y. F. Zhu, *Chem. Mater.* **2005**, *17*, 3537.
[11] J. H. Bang, R. J. Helmich, K. S. Suslick, *Adv. Mater.* **2008**, *20*, 2599.
[12] Y. F. Sun, C. Z. Wu, R. Long, Y. Cui, S. D. Zhang, Y. Xie, *Chem. Commun.* **2009**, 4542.
[13] P. Wang, B. B. Huang, X. Y. Qin, X. Y. Zhang, Y. Dai, J. Y. Wei, M. H. Whangbo, *Angew. Chem.* **2008**, *120*, 8049; *Angew. Chem. Int. Ed.* **2008**, *47*, 7931.
[14] X. Wang, K. Maeda, A. Thomas, K. Takanabe, G. Xin, K. Domen, M. Antonietti, *Nat. Mater.* **2009**, *8*, 76.
[15] Y. J. Lin, S. Zhou, X. H. Liu, S. Sheehan, D. W. Wang, *J. Am. Chem. Soc.* **2009**, *131*, 2772.
[16] Z. G. Zou, J. H. Ye, K. Sayama, H. Arakawa, *Nature* **2001**, *414*, 625.
[17] K. Maeda, K. Teramura, D. Lu, T. Takata, N. Saito, Y. Inoue, K. Domen, *Nature* **2006**, *440*, 295.
[18] D. F. Wang, T. Kako, J. H. Ye, *J. Am. Chem. Soc.* **2008**, *130*, 2724.
[19] J. G. Hou, Y. F. Qu, D. Krsmanovic, C. Ducati, D. Eder, R. V. Kumar, *Chem. Commun.* **2009**, 3937.
[20] Z. Y. Liu, D. D. Sun, P. Guo, J. O. Leckie, *Chem. Eur. J.* **2007**, *13*, 1581.
[21] J. G. Yu, Y. R. Su, B. Cheng, *Adv. Funct. Mater.* **2007**, *17*, 1984.
[22] X. H. Sun, C. M. Zheng, M. Q. Qiao, J. J. Yan, X. P. Wang, N. J. Guan, *Chem. Commun.* **2009**, 4750.
[23] W. Fan, M. A. Snyder, S. Kumar, P. S. Lee, W. C. Yoo, A. V. McCormick, R. L. Penn, *Nat. Mater.* **2008**, *7*, 984.
[24] F. Ocampo, H. S. Yun, M. M. Pereira, J. P. Tellonnier, B. Louis, *Cryst. Growth Des.* **2009**, *9*, 3721.
[25] H. X. Li, Z. F. Bian, J. Zhu, D. Q. Zhang, G. Li, Y. Huo, H. Li, Y. F. Lu, *J. Am. Chem. Soc.* **2007**, *129*, 8406.
[26] J. F. Qian, P. Liu, Y. Xiao, Y. Jiang, Y. L. Cao, X. P. Ai, H. X. Yang, *Adv. Mater.* **2009**, *21*, 3663.
[27] A. Imhof, D. J. Pine, *Nature* **1997**, *389*, 948.
[28] O. D. Velev, E. W. Kaler, *Adv. Mater.* **2000**, *12*, 531.
[29] M. Breulmann, S. A. Davis, S. Mann, H. P. Hentze, M. Antonietti, *Adv. Mater.* **2000**, *12*, 502.
[30] a) X. M. Sun, Y. D. Li, *Angew. Chem.* **2004**, *116*, 607; *Angew. Chem. Int. Ed.* **2004**, *43*, 597; b) H. S. Qian, M. Antonietti, S. H. Yu, *Adv. Funct. Mater.* **2008**, *18*, 637; c) X. M. Sun, J. F. Liu, Y. D. Li, *Chem. Eur. J.* **2006**, *12*, 2039.
[31] D. K. Ma, M. Zhang, G. Xi, J. H. Zhang, Y. T. Qian, *Inorg. Chem.* **2006**, *45*, 4845.
[32] C. J. Murphy, N. R. Jana, *Adv. Mater.* **2002**, *14*, 80.
[33] N. R. Jana, L. Gearheart, C. J. Murphy, *J. Phys. Chem. B* **2001**, *105*, 4065.
[34] M. M. Titirici, M. Antonietti, A. Thomas, *Chem. Mater.* **2006**, *18*, 3808.

Received: December 9, 2009
Revised: April 7, 2010
Published online: June 23, 2010

